





Cite this: DOI: 10.1039/d3ta01707a

Self-standing TiC-modified carbon fibre electrodes derived from cellulose and their use as an ultrahigh efficiency lithium metal anode†

Junren Wang, Huimian Zhong, Bowen Liu, Min Zhang, Andrew L. Hector * and Andrea E. Russell 

Lithium metal anodes could be a key component of high energy density rechargeable batteries, but uncontrolled growth of Li dendrites, large volume expansion, and unstable solid electrolyte interface films seriously hinder the practical applications of Li metal batteries. In this work, a self-standing three-dimensional TiC-modified carbon fibre (TiC@C) network has been fabricated by carbothermal reduction. Binding energy calculations reveal that Li is preferentially plated on TiC rather than the bare C skeleton. The lithiophilic TiC not only serves as a Li nucleation site to assist homogeneous Li deposition, but it also enables rapid Li deposition due to its high electronic conductivity. The 3D conductive structures with high surface area play an important role in reducing the local current density, and also accommodate Li volume changes during repeated cycling. As a result, the TiC@C electrode achieves a nearly zero Li nucleation overpotential and low voltage hysteresis of 150 mV at 2 mA cm⁻². Passing 1 mA h cm⁻² charge, the coulombic efficiency (CE) was found to be 99.6% over more than 200 cycles. Furthermore, full cells assembled with a LiFePO₄ cathode in a conventional carbonate electrolyte achieve an impressive capacity retention of 87% over 250 cycles. This work demonstrates a novel design of a 3D lithiophilic host for dendrite-free lithium metal anodes.

Received 22nd March 2023
Accepted 26th June 2023

DOI: 10.1039/d3ta01707a

rsc.li/materials-a

Introduction

With the ever-increasing requirement for high energy density batteries, graphite, the traditional anode material for lithium-ion batteries (LIBs), is close to its theoretical capacity limit of 372 mA h g⁻¹.¹ Lithium metal (Li) is the optimum anode material for high energy density rechargeable batteries due to its high theoretical specific capacity of 3860 mA h g⁻¹ and a low redox potential of -3.04 V vs. SHE.^{2,3} However, unstable solid electrolyte interphase (SEI) formation, a large volume expansion during cycling and uncontrolled growth of lithium dendrites lead to a low coulombic efficiency (CE), a short cycle life and safety concerns. These factors seriously hinder its practical applications.⁴

Tremendous efforts have been made to solve the key issues with lithium metal batteries (LMBs), including modifying the liquid electrolyte with additives or adjusting Li salts to construct stable SEI layers;⁵ applying novel gel or solid-state electrolytes as mechanical barriers to limit the growth of lithium dendrites;^{6,7} and designing SEI layers to inhibit lithium dendrites by physical or chemical methods.^{8,9} Recently, constructing a three-

dimensional (3D) structured substrate as a “host” for lithium metal to reduce local currents and hence the tendency to form dendrites, while alleviating the effects of volume expansion, has delivered enhancements in the cycling performance of LMBs.^{10,11} Compared with metal skeletons, carbon materials such as mesoporous carbon,¹² carbon nanotubes,¹³ graphene¹⁴ and biomass-derived carbons are attractive hosts for lithium metal anodes as they are lightweight and possess high surface area, high mechanical strength and flexibility.^{12,15} In addition, biomass carbon materials are environmentally friendly and cost-effective compared to other synthetic materials, which is important for large-scale industrial production.¹⁶ It is still difficult to obtain a uniform Li deposition on carbon skeletons at higher current densities and capacities because of the low affinity between bare carbon and Li induced by the lattice mismatch.¹⁷ Li ions tend to be deposited on the top surface of the 3D skeleton, resulting in additional loose Li dendrites and a decrease in the cyclability of the Li metal anode.

Lithiophilic modifications (*e.g.*, metal seeds,¹⁸ element doping^{19,20} and transition metal compounds^{21–26}) have been used to improve the affinity between Li and substrates.²⁷ Transition metal carbides (TMCs) have high conductivity and are considered to be promising lithiophilic materials.^{25,26,28} Yu *et al.*²⁶ used Mo₂C quantum dots anchored on N-doped graphene to achieve fast diffusion pathways for Li⁺ ion transport and uniform Li deposition. Yang *et al.*²⁸ also found that

School of Chemistry, University of Southampton, SO17 1BJ, UK. E-mail: A.L.Hector@soton.ac.uk

† Electronic supplementary information (ESI) available. See DOI: <https://doi.org/10.1039/d3ta01707a>



lithiophilic iron carbide can guide lithium ions to diffuse in the interlayers of carbon nanotubes. Liu *et al.*²⁸ prepared carbon-coated TiC nanowire anodes by CVD onto a Ti₆Al₄V foil and infused them with molten Li metal at >300 °C. In this system the TiC core provides the advantage of excellent electrical conductivity and abundant porosity of the resultant TiC/C array and hence obtained advantageous behaviour, but the surface is still carbon so the lithiophilicity advantage is not maximised. The molten Li infusion also poses some safety concerns,²⁹ and is difficult to implement on a large scale.

Herein, a 3D structured self-standing lithium metal anode was produced with TiC nanoparticles decorated onto carbon fibres (TiC@C) *via* a carbothermal reduction of modified cellulose fibres. The abundant hydroxyl groups on the cellulose polymer chains provide many modification possibilities to improve the lithiophilicity.^{30,31} The electrochemical properties and mechanism of TiC@C were compared experimentally and theoretically with a C skeleton. It was intended that the lithiophilic TiC would provide Li nucleation sites to assist homogeneous Li deposition as well as improving conductivity, hence the TiC was grown at the surface of the fibres. The performance of the TiC@C fibres were tested with various TiC loadings. The TiC@C electrodes achieved a nearly zero Li nucleation overpotential and low voltage hysteresis of 150 mV at 2 mA cm⁻². With 1 mA h cm⁻² total charge passed during lithiation, charge and discharge were carried out over more than 200 cycles with a high coulombic efficiency (CE) of around 99.6%. Prelithiation *via* electrochemical deposition not only effectively controls the deposition capacity of lithium metal, but also allows the observation of changes in the electrochemical performance by adjusting the electrochemical deposition conditions (*e.g.*, amount of Li deposition and rate of Li deposition). The Li@TiC@C anode produced by electrochemical deposition of lithium onto TiC@C exhibits excellent cycling stability and small voltage hysteresis in symmetric cells and full cells when coupled with a LiFePO₄ cathode.

Experimental section

The TiC@C composites were synthesised by reacting filter paper with TiCl₄, then the paper was carbonised in the tube furnace under an Ar atmosphere emulating a process we recently used to make TiC@C powders.³⁰ In brief, 2 pieces of filter paper (24.0 cm, Whatman, CAT. No. 1001-240) were cut into strips (2 cm width). 5 g of filter paper strips were washed with deionised water three times and dried in an oven at 120 °C overnight. Then, 0.44 mL, 0.66 mL or 0.88 mL of TiCl₄ (Sigma-Aldrich, 99.9% trace metals basis) was dissolved in hexane (400 mL, Fisher Scientific, distilled from sodium/benzophenone ketyl ether) and stirred for 30 min at room temperature to prepare a 0.01, 0.015 or 0.02 mol dm⁻³ TiCl₄ solution. The dried filter papers were then added into the solution. After refluxing the mixture at 80 °C overnight, the solvent and any remaining precursor were removed *in vacuo*. The dried material was carbonised at 1400 °C for 2 h under flowing argon with a temperature ramp rate of 4 °C min⁻¹. A pure carbon sample

was synthesised by the direct carbonisation of dried filter paper at 1400 °C for 2 h without any modifying operations.

Powder X-ray diffraction (XRD) patterns were obtained in 0.6 mm silica capillaries using a Rigaku Smartlab with Cu-K_α X-rays and a Hypix detector in 1D mode. XRD data analysis used the Rigaku PDXL-2 package. Thermogravimetric analysis (TGA) was performed using a Netzsch TG 209 F1 Libra with a ramp rate of 10 °C min⁻¹ and a flowing gas combination of Ar (50 mL min⁻¹) and O₂ (20 mL min⁻¹). Scanning electron microscopy (SEM) was performed using a Philips XL30, a Jeol JSM6500 and ZEISS Sigma 500VP PE with a 10 kV accelerating voltage. The surface areas were determined using the Brunauer–Emmett–Teller (BET) technique based on nitrogen adsorption and desorption isotherms measured on a Micromeritics Tristar II surface area analyzer.

The working electrodes were formed by punching the samples directly into 11 mm diameter discs with average mass of 2.6 mg. Lithium metal was used as the counter and reference electrode. Two sheets of dried Whatman GF/D glass fibre (GE Healthcare Life Sciences) were used as the separator. 1 mol dm⁻³ LiTFSI in dimethoxyethane (DME)/1,3-dioxolane (DOL) (1 : 1, v/v) with 1 wt% LiNO₃ additive (Duoduo Chem Ltd) was used as the electrolyte for half cells and symmetric cells. The electrolyte for full cells was 120 μL of 1 mol dm⁻³ LiPF₆ in ethylene carbonate (EC)/diethyl carbonate (DEC) (1 : 1, v/v) (Duoduo Chem Ltd). Swagelok cells assembled in an argon-filled glovebox (Belle, H₂O < 0.1 ppm, O₂ < 0.1 ppm) were used for all the electrochemical tests. Biologic BCS-805 and SP-150 potentiostats were used to conduct electrochemical measurements with temperature maintained at 25 °C with a Memmert IPP 55 Plus climatic chamber.

The coulombic efficiency of Li plating and stripping were measured with Li half cells at a current density of 2 mA cm⁻² with charge calculated for an area capacity of 1 mA h cm⁻². All half cells were first cycled at 0–1 V at a small current density (50 μA) for 5 cycles to stabilise the SEI film and remove surface contamination. After that, a particular quantity of Li was plated on the working electrodes under a constant current density for a certain length of time, and then the electrodes were stripped at the same current density with a cut-off voltage of 1.0 V. Coulombic efficiency (CE) was determined by dividing the lithium stripping capacity by the Li plating capacity for each cycle. Electrochemical impedance spectroscopy (EIS) was obtained in the frequency range from 0.01 Hz to 10 kHz.

For the symmetric cells and full cells, lithium was firstly electrochemically deposited in a half cell onto the electrodes' surface to a charge of 6 mA h cm⁻² at a current density of 0.5 mA cm⁻². Then for symmetric cells, both sides are plated anodes or Li foil. For full cells, TiC@C electrodes plated with 6 mA h cm⁻² Li (Li@TiC@C) were used as the anode, and commercial LiFePO₄ (Qinetiq Tatung, C coated) with an areal capacity of 1.68 mA h cm⁻² was used as the cathode to investigate the practical applications of Li@TiC@C anodes. The LiFePO₄ powder was mixed with Super P (carbon black) and polyvinylidene difluoride (PVDF, Solvay) in *N*-methyl pyrrolidone (NMP, anhydrous, 99.5%, Sigma-Aldrich) with a mass ratio of 8 : 1 : 1. Then, the slurry was mixed with a homogeniser



(running at speeds of 10 000, 15 000, and 20 000 rpm for 5, 3, and 2 min, respectively) followed by casting onto aluminium foil (15 μm thick, Goodfellow Cambridge Ltd). The ink was air-dried, cut into 11 mm diameter discs and pressed under 5 tonnes pressure. All the electrodes were dried under vacuum overnight at room temperature before use. In the full cell tests, 1C was defined as 170 mA g^{-1} based on the theoretical capacity of LiFePO_4 .

Results and discussion

The main component of the filter papers is cellulose, whose hydroxide groups are expected to react with the TiCl_4 precursor to generate C–O–Ti bonds with HCl as the by-product.³⁰ Different amounts of TiCl_4 (Table 1) were added to produce composites with various TiC loadings. After sintering, composites of TiC with a self-standing carbon skeleton were obtained. The crystal structures of the samples were characterised by XRD (Fig. 1a). All the patterns show a broad peak around 23° corresponding to the 002 reflection of the graphitic domains of the carbon, and a second broad peak at around 44° corresponding to the 100 peak. In the TiC composite, the intensity of the 111, 200, and 220 peaks of TiC increase as the titanium content increases. The obtained rock-salt-type patterns for the cubic TiC were refined to give the lattice parameters, shown in Table 1 (data refinement can be found in

Fig. S1, ESI†). The lattice parameters are compared with the data reported in the Inorganic Crystal Structure Database (ICSD). After carbonisation in argon, it is evident that all of the composites had lattice parameters similar to the ICSD values for TiC (all close to 4.31 Å). The carbon can only come from the cellulose in this synthesis, so this suggests that TiC was in direct contact with the surface of the carbon fibres. Meanwhile, the diffraction peaks become narrower as the TiC loading increases, implying that the crystallite sizes become larger.³⁰ The crystallite size of TiC evaluated from the diffraction data varies from 7 to 40 nm as reported in Table 1.

The TiC contents of the composites were calculated by TGA (Fig. S2, the calculation process can be found in ESI†), and the results are provided in Table 1. After analysis and calculation, the fraction of TiC in TiC@C1, TiC@C2, and TiC@C3 were found to be 9.5 wt%, 22.9 wt%, and 32.4 wt%, respectively. N_2 adsorption-desorption measurements (Fig. 1b and Table 1) show a typical type-IV behaviour, indicating the presence of mesoporosity.³²

The Brunauer-Emmett-Teller (BET) analysis reveals a specific surface area of 27 $\text{m}^2 \text{g}^{-1}$ for TiC@C1 and 22 $\text{m}^2 \text{g}^{-1}$ for TiC@C3, which are both higher than that of the bare C electrode (9 $\text{m}^2 \text{g}^{-1}$). TiC@C2 showed the highest surface area of 58 $\text{m}^2 \text{g}^{-1}$. The extra surface area could be attributed to the TiC particles, or to the reaction between the titanium chloride and

Table 1 Physical parameters of C and TiC@C composites

Sample name	TiCl_4 volume/mL	TiC/Å	TiC crystallite size/Å	Surface area/ $\text{m}^2 \text{g}^{-1}$	Pore volume/ $\text{cm}^3 \text{g}^{-1}$
C	0	n/a	n/a	9	0.0001
9.5 wt% TiC@C1	0.44	4.31(5)	70(3)	27	0.0095
22.9 wt% TiC@C2	0.66	4.31(3)	324(7)	58	0.0243
32.4 wt% TiC@C3	0.88	4.31(6)	396(2)	22	0.0166

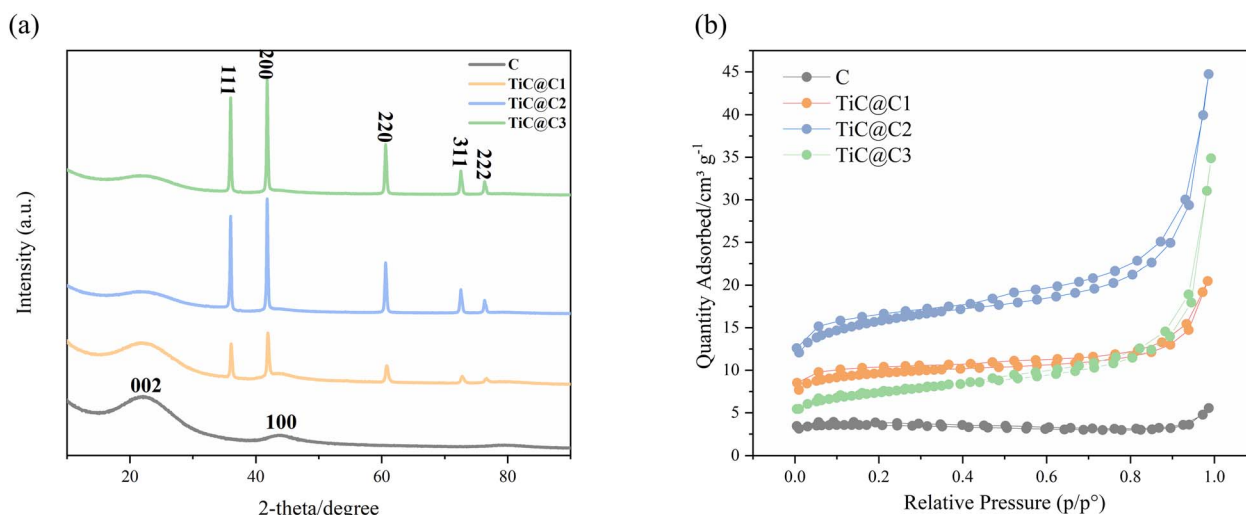


Fig. 1 (a) XRD patterns of C (black line), 9.5 wt% TiC@C1 (orange line), 22.9 wt% TiC@C2 (blue line) and 32.4 wt% TiC@C3 (green line); (b) the nitrogen adsorption-desorption isotherms of C, TiC@C1, TiC@C2 and TiC@C3.



the cellulose roughening the surface of the carbon fibres. When further increasing the added volume of TiCl_4 , the reduced surface area of TiC@C3 may be due to the covering or filling of mesopores of the carbon skeleton.³⁰ Constructing a 3D structure with a large surface area as lithium host has been demonstrated to be an efficient way to reduce local current density, which is advantageous for inhibiting the formation of dendritic Li, according to Sand's model.^{33,34} In addition, the 3D network with a large amount of void space is able to store more Li while also limiting the volumetric fluctuation of the anode during cycling. TiC@C2 also provides a larger pore volume (Table 1) than that of TiC@C3 , TiC@C1 and bare C. The pore size distribution (Fig. S3, ESI[†]) shows TiC@C2 has the largest amount of mesopores (>2 nm) among the three samples. Mesopores are more conducive to the penetration of an electrolyte than micropores (<2 nm), which is beneficial for reducing charge-transfer resistance.²⁰

Fig. S4a (ESI[†]) displays a photograph of the commercial laboratory filter paper. After TiC modification and annealing at 1400 °C under Ar atmosphere, the obtained TiC@C papers exhibit good mechanical strength and are easy to punch into disks as electrodes for electrochemical tests (Fig. S4b, ESI[†]). The SEM data in Fig. 2a show that the bare C retains the interlinked 3D structure of the cellulose without visible deterioration after carbonisation at 1400 °C. The magnified structure (Fig. 2b) exhibits a smooth carbon surface. As a conductive network, the intact cross-linked carbon framework may help to homogenise the electric field generated during the Li deposition process.³⁵ The TiC decorated electrodes (Fig. 2c–h) have TiC nanoparticles coated onto the surface of the carbon skeletons. In general, as the amount of the TiCl_4 precursor added increases, the number of the obtained TiC particles also gradually increases, which is consistent with the TGA results. This can increase the specific surface area, compared to that of bare C. When synthesising TiC@C1 in a lower TiCl_4 concentration, as shown in Fig. 2c, the distance between the formed TiC particles is larger. Another point that should be noticed is that there are holes evenly distributed on the C skeleton after the TiC surface modification (Fig. 2d). This might be related to the by-product HCl during the synthesis process or to the carbothermal reduction process. The TiC particles in TiC@C1 are decorated on the surface of the C, rather than in the holes. This will increase the surface area of the composite material, which is consistent with BET results. TiC@C2 obtained from a higher TiCl_4 concentration exhibits a denser covering of TiC nanoparticles in Fig. 2e. The surface of the C skeleton in TiC@C2 has been further roughened (Fig. 2f), which results in a higher surface area in combination with the nanoparticles. These TiC nanoparticles can be observed homogeneously decorated on the carbon skeleton in the Ti elemental mapping image (Fig. S5[†]). However, when continuing to increase the TiCl_4 concentration to fabricate TiC@C3 , TiC particles aggregate in regions of the C skeleton rather than being uniformly distributed on the C surface (Fig. 2g). These TiC particles are observed in the rough gaps and also cover these gaps (Fig. 2h), which leads to the reduced surface area of TiC@C3 compared with TiC@C2 .

The capability of TiC@C and bare C skeleton as a Li host and the deposition behaviour were first investigated in a Li half-cells, *i.e.* with TiC@C as the working electrode and Li foil as the counter and reference electrode. Fig. 3a shows the first reduction voltage profiles of the bare C electrode and TiC@C composite electrodes with different mass ratios of TiC under a current density of 2 mA cm^{-2} and a lithium plating capacity of 1 mA h cm^{-2} . During the initial stages of reduction from 1 to 0 V, there is a slanted voltage profile, indicating that Li^+ ions are gradually inserted. This behaviour is similar to the Li intercalation behaviour previously reported for self-standing carbonised filter paper electrodes.²⁰ Li intercalation may increase the lithiophilicity of the carbon and TiC@C electrodes.³⁶

When the voltage drops below 0 V, Li starts to be plated into the anodes. The TiC@C2 electrode exhibits the lowest overpotential (-60 mV), while the overpotentials of bare C and TiC@C1 electrodes are -180 mV and -86 mV. During the Li plating process, the overpotential can be separated into two parts: (i) the mass-transfer overpotential, which is connected to Li^+ diffusion to the electrode surface; (ii) the Li nucleation overpotential, which is related to the lithiophilicity of the electrodes. The overpotential for Li nucleation is defined as the voltage difference between the lowest point of the curve and the subsequent plateau.³⁷ Fig. 3b enlarges the part profiles and shows that the TiC@C2 electrode exhibits nearly no nucleation overpotential. The TiC@C1 electrode has a low Li nucleation overpotential of 7 mV, while the nucleation overpotential of the C electrode (-23 mV) is nearly three times higher than that of the TiC@C1 electrode. The value of nucleation overpotential is related to the particle size, the mass ratio of active material and homogeneity on the substrate.^{18,32} The zero nucleation overpotential of the TiC@C2 electrode could be ascribed to the 3D cross-linked structure with the highest surface area of these samples, which reduces the local current density for a given applied current. Reducing the local current density on the substrate surface is critical to retard the growth of lithium dendrites.²⁴ Meanwhile, the lithiophilic TiC effectively improves the affinity between the entire 3D electrode and Li, leading to a lower Li nucleation barrier and regulating Li deposition behaviour. The suitable particle size of TiC with a uniform distribution on the surface of carbon skeleton can further reduce the nucleation overpotential to zero. The voltage hysteresis is defined as the difference between the lithium plating and stripping voltages, which is primarily influenced by the current density, charge transfer resistance, and interface properties of the electrode during lithium plating and stripping.³⁸ As shown in Fig. 3c, the TiC@C2 electrode shows the lowest voltage hysteresis of 150 mV much lower than the bare C electrode of 590 mV and the TiC@C1 of 240 mV, demonstrating the TiC@C2 electrode has the most uniform Li^+ flux. The lack of lithiophilic active sites on the surface of the C electrode leads to the nonuniform deposition of lithium. The introduction of TiC reduces the electrochemical polarisation of the deposition process, allowing the lithium to be uniformly distributed and deposited on the surface of the TiC@C composite electrode. In subsequent cycles, the lithiation behaviour of the bare carbon electrode undergoes a rapid degradation in the 38th cycle and



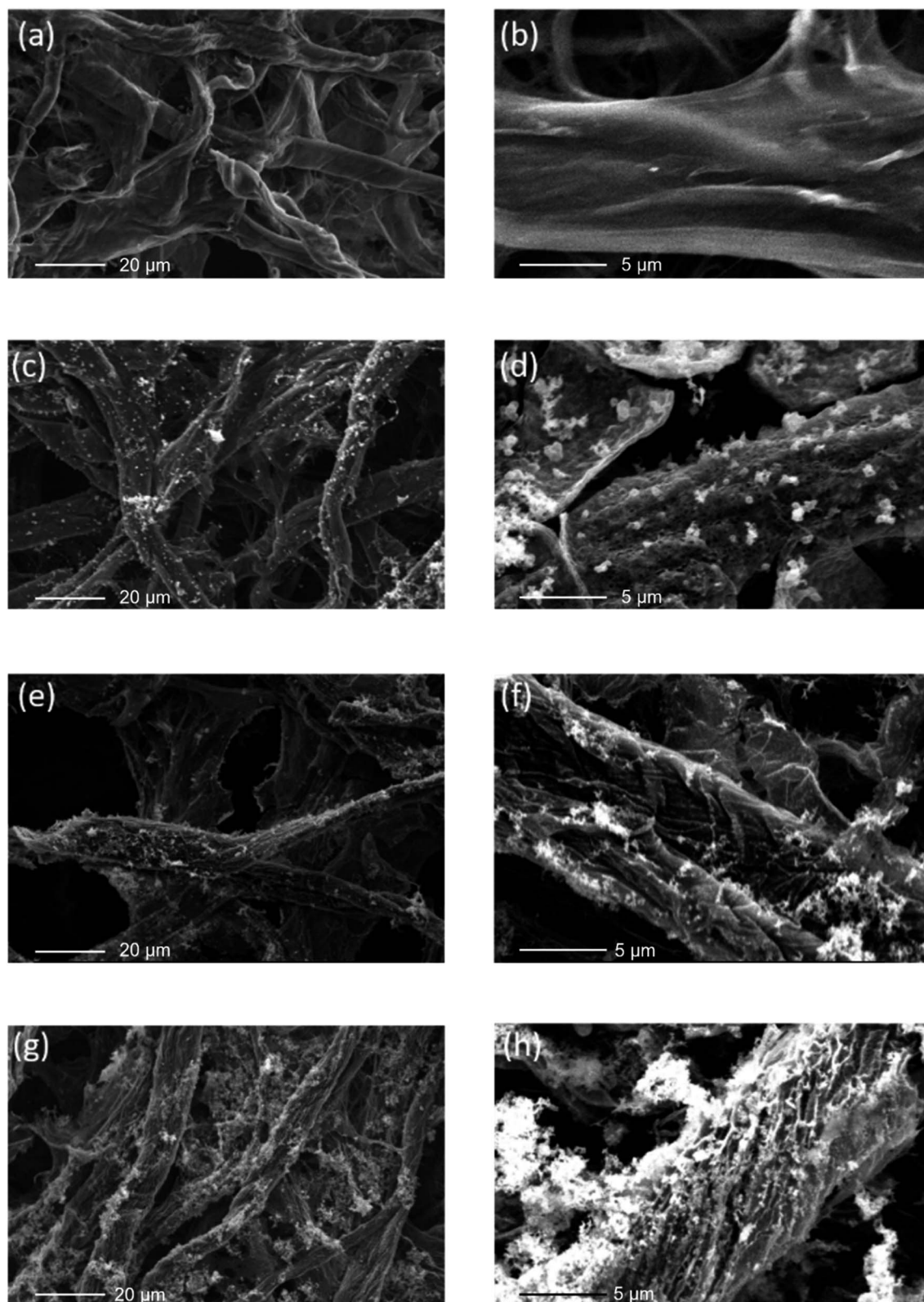


Fig. 2 SEM images of (a and b) C; (c and d) 9.5 wt% TiC@C1; (e and f) 22.9 wt% TiC@C2; (g and h) 32.4 wt% TiC@C3. The scale bar is 20 μm in the left-hand images and 5 μm in the right-hand ones.



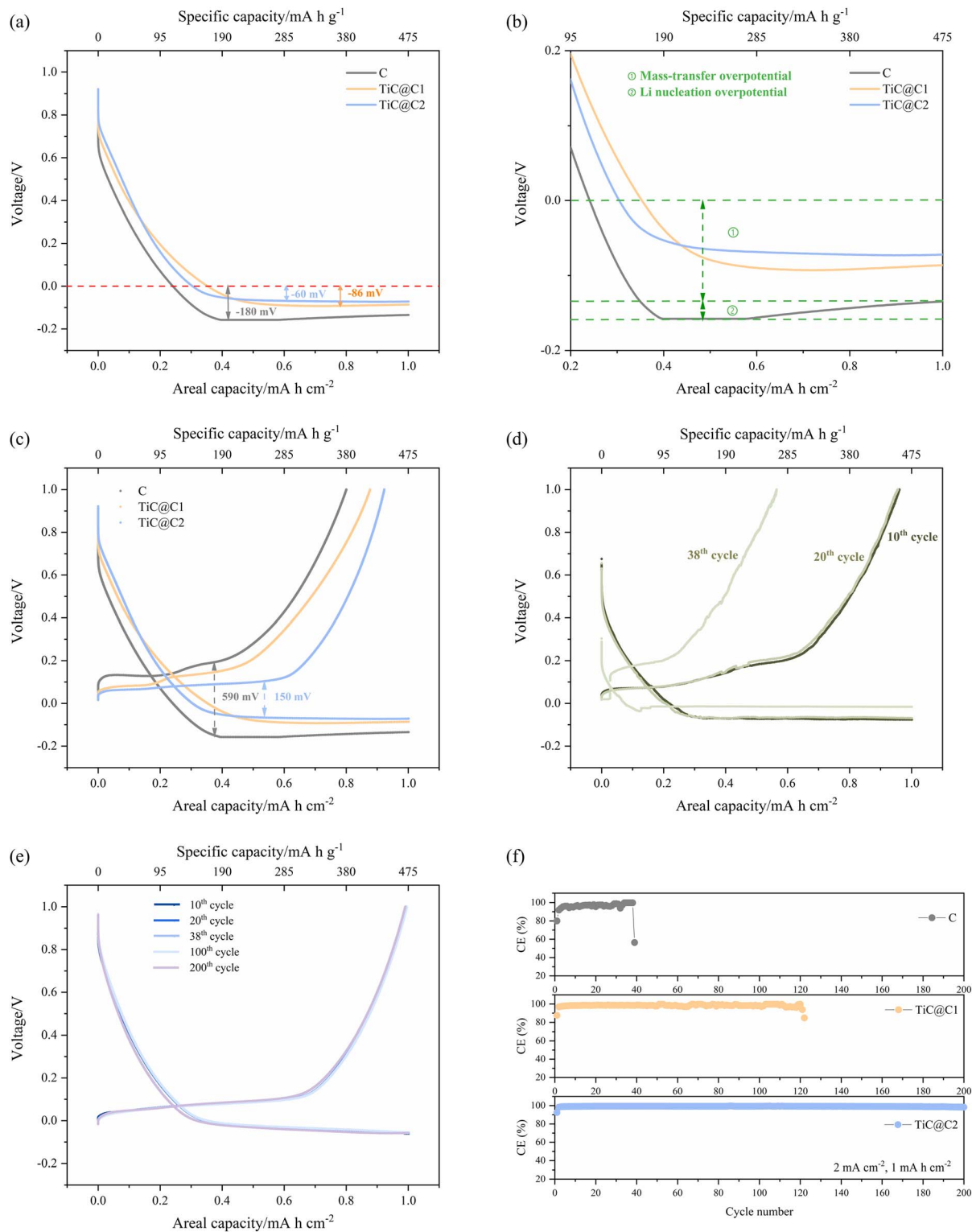


Fig. 3 (a) 1st cycle reduction curves of different electrodes under a current density of 2 mA cm⁻² with a lithium plating capacity of 1 mA h cm⁻²; (b) enlarged section of the data shown in (a); (c) voltage profiles of the 1st cycle of different electrodes under a current density of 2 mA cm⁻² with a lithium plating capacity of 1 mA h cm⁻²; comparison of voltage profiles of the Li plating/stripping (d) on the bare C electrode, (e) on the TiC@C2 electrode at different cycles. (f) CE comparison of bare C, TiC@C1, and TiC@C2 electrodes measured at a current density of 2 mA cm⁻² with a lithium plating capacity of 1 mA h cm⁻².



the rough voltage profile is indicative of the uncontrolled growth of Li dendrites (Fig. 3d). In contrast, the TiC@C2 electrode retains a steady Li^+ insertion/extraction behaviour at 0–1 V and low voltage hysteresis during the repeated Li plating/stripping process over 200 cycles (Fig. 3e). These findings above indicated that TiC improved the lithium affinity of the C-based electrode and decreased the lithium nucleation energy barrier.

The cycling performance of the bare C electrode and the composite electrodes with different mass loadings of TiC were compared in Fig. 3f (with repeat tests in Fig. S6, ESI†). The cells were tested at a current density of 2 mA cm^{-2} with a specific plating/stripping capacity of 1 mA h cm^{-2} . For the bare C electrode, the CE was maintained at 95% for only 38 cycles then dropped abruptly, suggesting the poor natural lithophilicity of the C electrode limited the reversibility of Li plating/stripping during cycling, leading to accumulation of dendritic and dead

Li. In contrast, the TiC@C1 electrode showed an average CE of approximately 98% over 100+ cycles, although these electrodes still failed after that. TiC@C2 shows the highest CE of approximately 99.6% over 200 cycles with a higher TiC mass loading and we did not experience failure of this type of electrode. Hence, a suitable amount of TiC nanoparticles can significantly improve the reversibility of metallic lithium deposition, a likely benefit of a lithophilic surface.

In order to verify the positive influence of TiC decoration for Li plating, density functional theory (DFT) calculations are employed to study the binding energy between Li atoms and TiC or bare C (Fig. 4a and b). The TiC (200) surface exhibits a stronger binding with Li atom (-2.43 eV) than that of C (-0.65 eV), which may explain the observation that Li^+ is reduced on the TiC more readily than the surface of C during the Li deposition process (Fig. 4c).

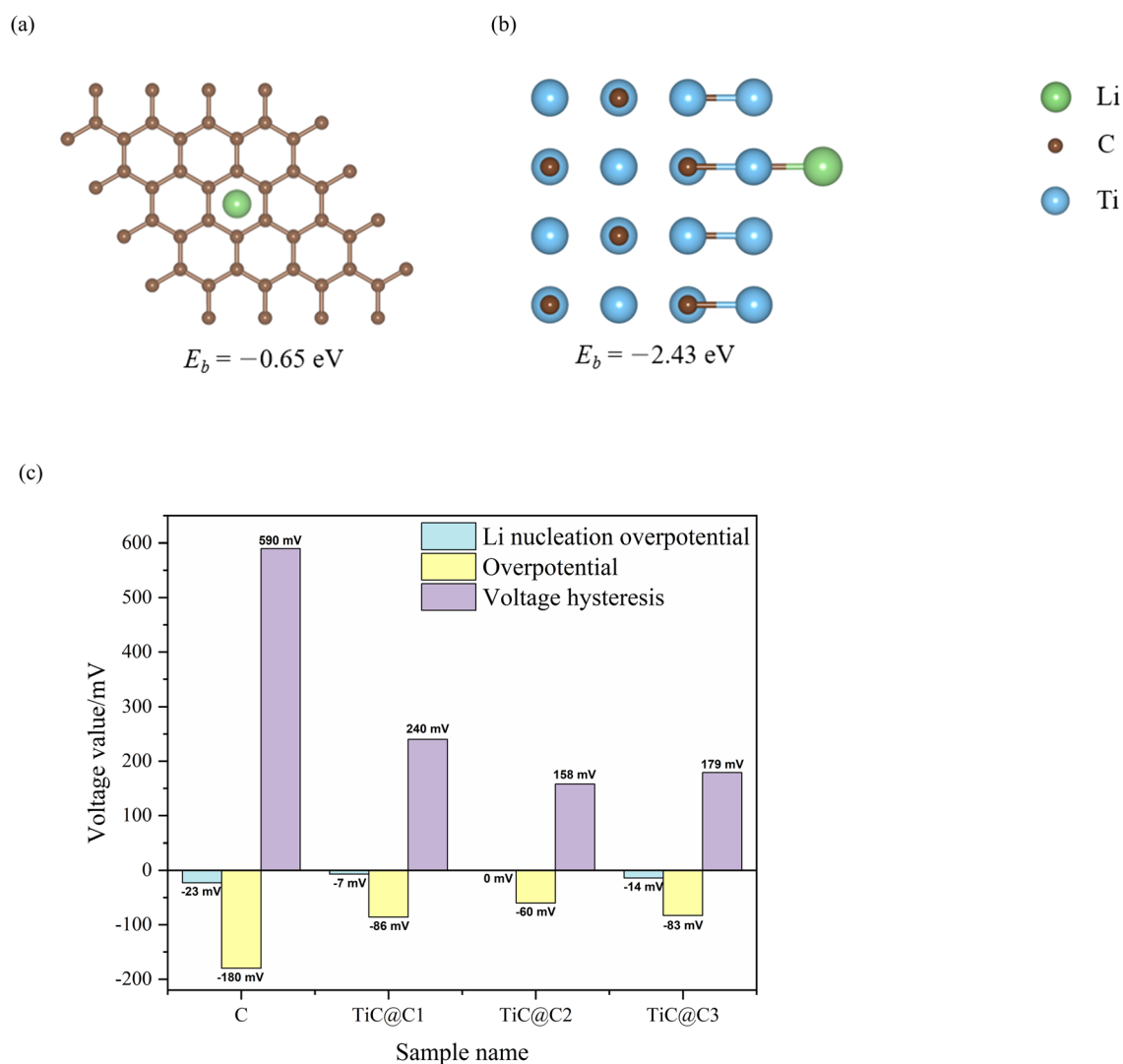


Fig. 4 Optimised geometries for calculating the binding energy of a Li atom adsorbed on (a) C; (b) TiC; (c) summary of the Li nucleation overpotential, overpotential and voltage hysteresis for different electrodes.



In order to give a further insight into the Li plating/stripping behaviour on different electrodes, a bare C electrode and a TiC@C2 electrode at different plating or stripping states were disassembled from half cells and washed with dry dimethoxyethane (DME) in the glove box. The function of TiC

nanoparticles in the Li nucleating and plating process is investigated using SEM. Illustrative images are shown in Fig. 5. Fig. 5b displays the Li nucleation and plating process on the bare C electrode. Due to the lattice mismatch between the body-centered cubic (bcc) structured lithium and hexagonal carbon,

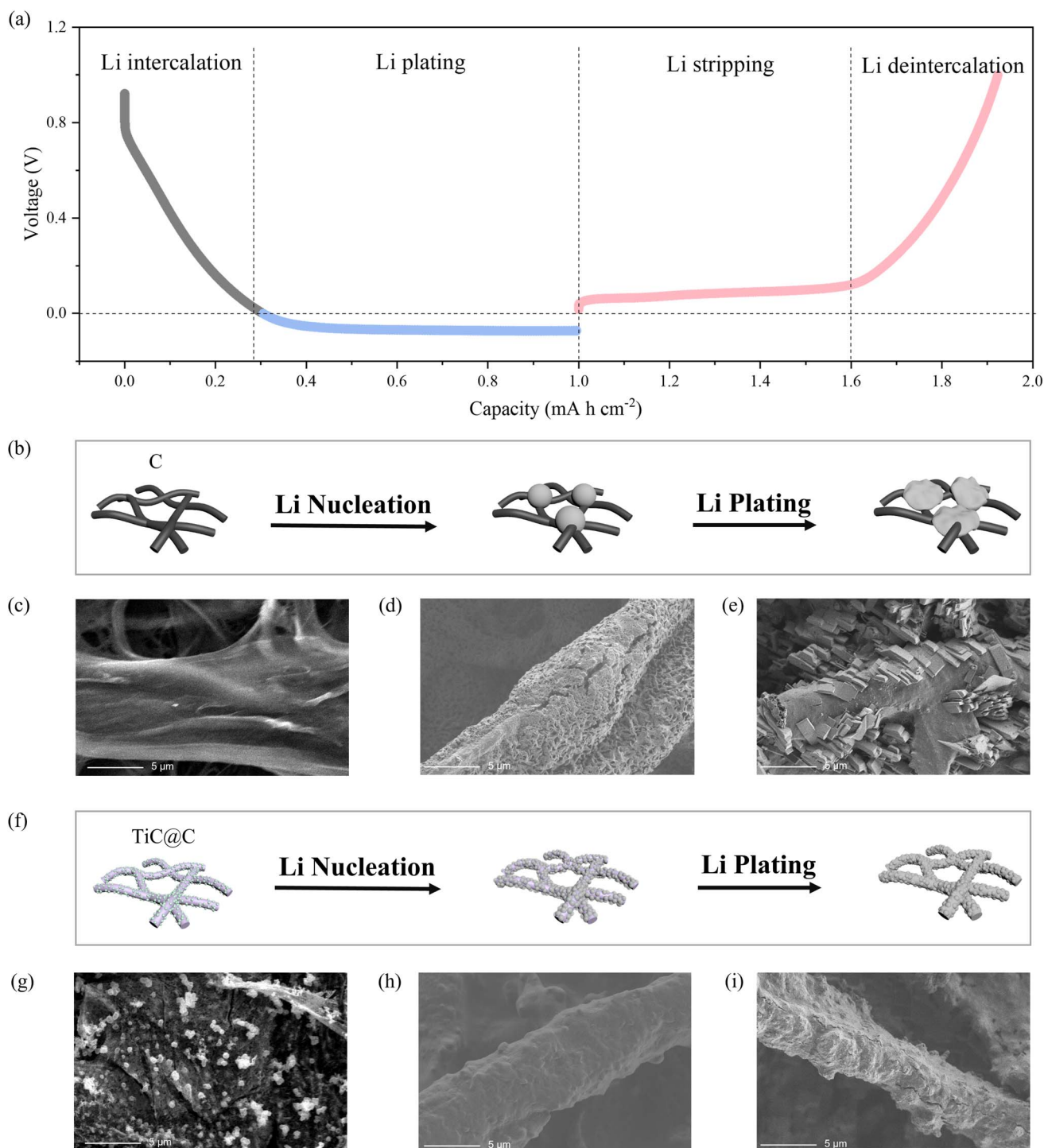


Fig. 5 (a) Voltage profile of TiC@C2 electrode during reduction and oxidation at a current density of 2 mA cm⁻² charged to a capacity of 1 mA h cm⁻²; different Li deposition behaviours (b) on the bare C electrode, (f) on the self-standing TiC@C2 electrode; top-view SEM images of (c) pristine C electrode, (d) C electrode after plating 1 mA h cm⁻² Li, (e) C electrode after plating 3 mA h cm⁻² Li, (g) pristine TiC@C2 electrode, (h) TiC@C2 electrode after plating 1 mA h cm⁻² Li, (i) TiC@C2 electrode after plating 3 mA h cm⁻² Li.



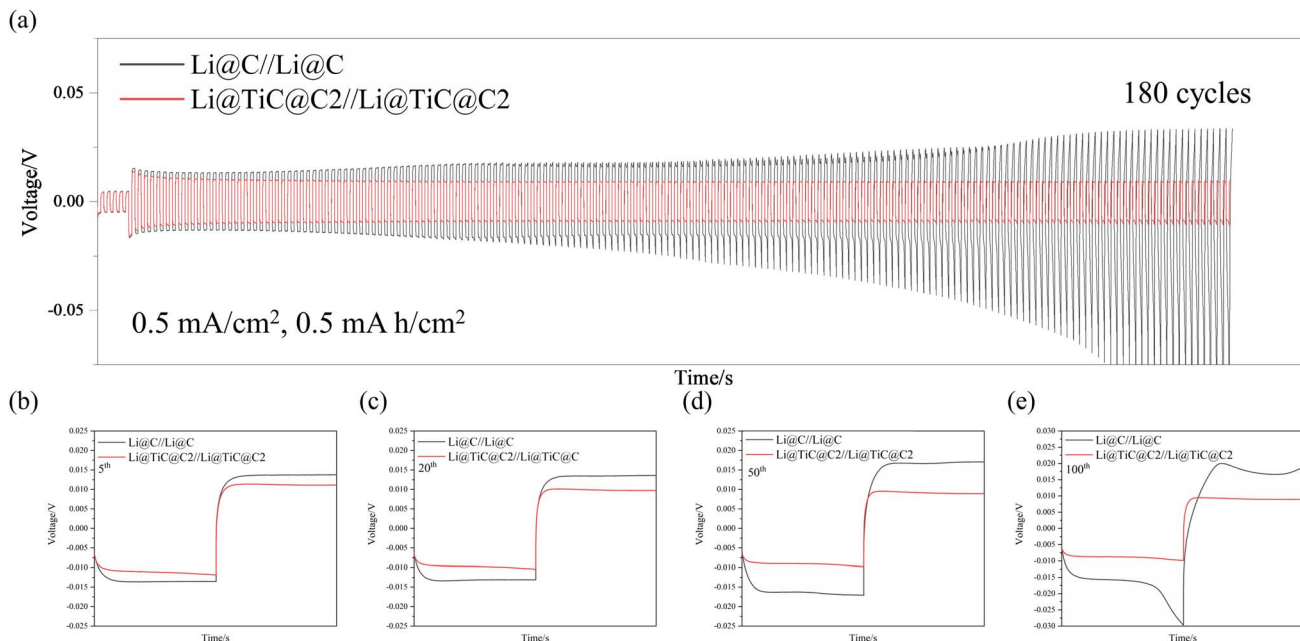


Fig. 6 (a) Voltage–time profiles of the symmetric cell with 0.5 mA h cm^{-2} capacity at 0.5 mA cm^{-2} ; enlarged typical profiles of the (b) 5th cycle; (c) 20th cycle; (d) 50th cycle and (e) 100th cycle.

Li tends to nucleate on junctions of linked fibres.³⁹ Fig. 5c shows the top-view morphology of a pristine C electrode without any Li plating. When the Li deposition capacity reaches 1 mA h cm^{-2} , as shown in Fig. 5d, the surface of the bare C electrode is quite rough. With further increase of the Li plating capacity to 3 mA h cm^{-2} , large Li crystallites can be found in Fig. 5e, suggesting growth from a small number of nucleation points. In contrast, in the case of self-standing TiC@C electrodes (Fig. 5f), the lithiophilic TiC offers abundant nucleation sites, regulating lithium deposition and inhibiting the growth of Li dendrites. After deposition of 1 mA h cm^{-2} Li, the TiC@C2 is uniformly covered by smooth Li (Fig. 5h), and even after a higher

deposition capacity of 3 mA h cm^{-2} , TiC@C2 is coated with uniform Li without any obvious Li dendrites (Fig. 5i). SEM characterisation was also employed to compare the structural features of TiC@C2 and bare C electrodes after 200 cycles

Table 2 EIS results of C and TiC@C2 after 10 cycles and 50 cycles

Sample	Cycle number	R_s/Ω	R_{ct}/Ω
C	10	5.3	9.9
TiC@C2	10	4.7	15.5
C	50	6.3	20.6
TiC@C2	50	5.1	14.7

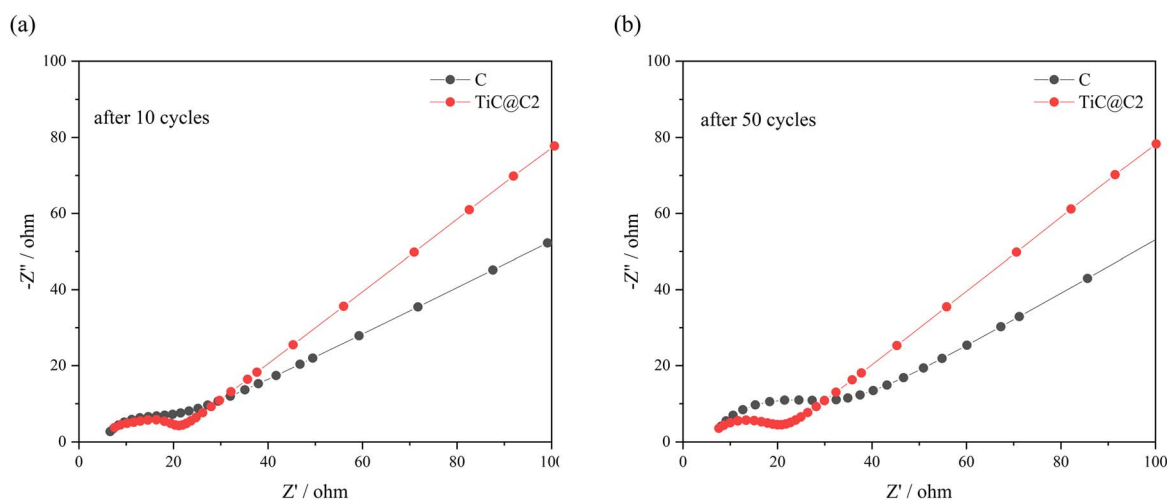


Fig. 7 EIS comparison between C cell and TiC@C2 cell (a) after 10 cycles; (b) after 50 cycles.



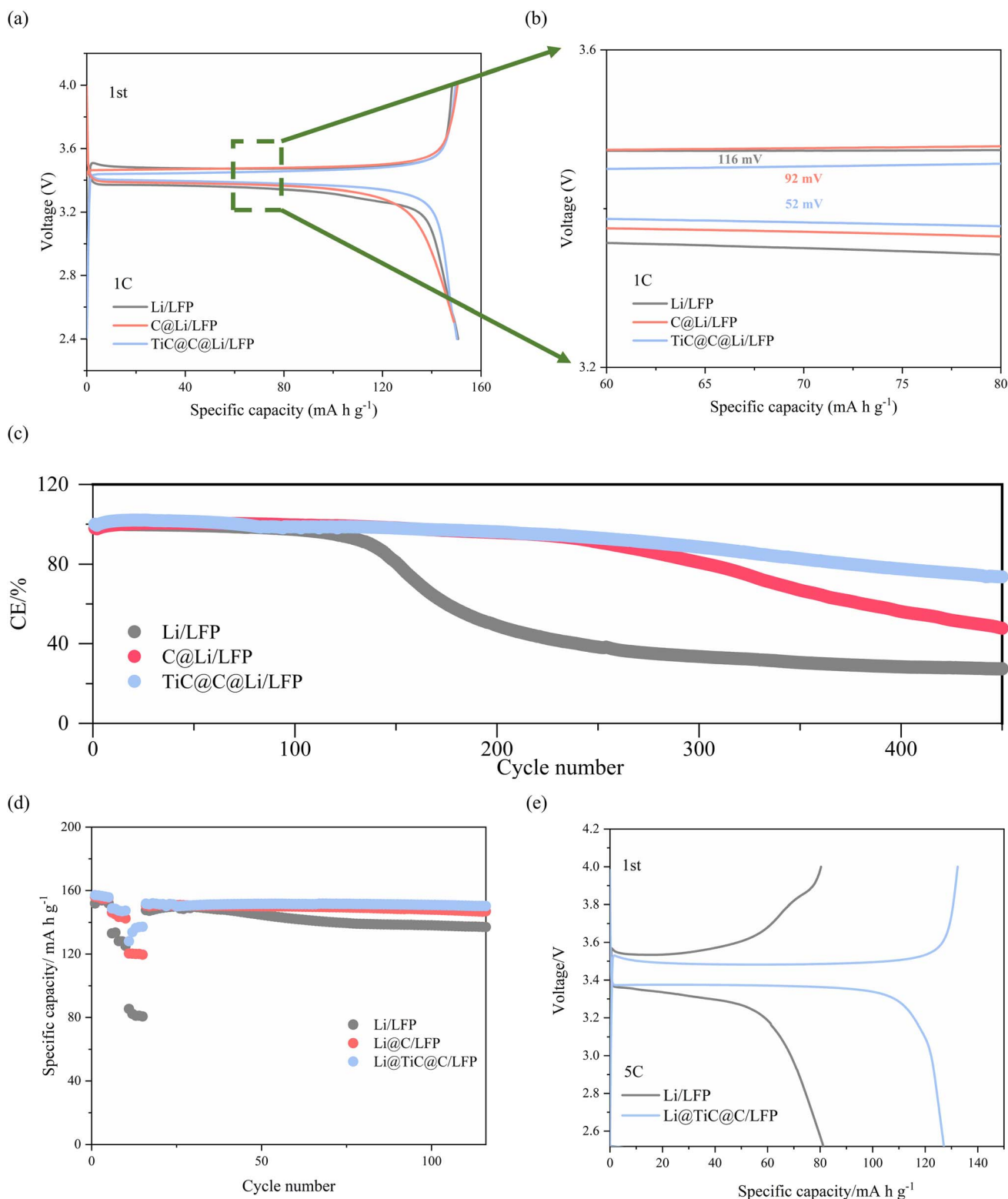


Fig. 8 (a) Typical charge/discharge profiles of full cells with LiFePO_4 as the cathode and Li foil, Li@C and Li@TiC@C as anodes at 1C; (b) enlarged part voltage profiles in (a); (c) cycling performance of full cells with different anodes at 1C; (d) rate capabilities of full cells with three different anodes (blue line for Li@TiC@C, red line for Li@C and black line for Li) coupled with LiFePO_4 cathodes; (e) first charge/discharge profiles of full cells with LiFePO_4 as the cathode and Li foil, Li@C and Li@TiC@C as anodes at 5C.



(Fig. S8†). In Fig. S8c,† TiC nanoparticles maintain a uniform distribution on the C skeleton after a long-time cycling, indicating an outstanding stability of this composite material due to a tight connection between TiC and C surface. The whole TiC@C2 anode preserves a clear cross-linked structure without any obvious formation of Li dendrites (Fig. S8d†). In contrast, the emergence of accumulated Li aggregation is shown on the surface of C skeleton, in Fig. S8a and b.† The formation of irreversible dead Li directly results in poor CE and cycling stability.

To investigate the difference in long-term cycling stability between the bare C and TiC@C2 electrodes, symmetric cells were used to observe the voltage variation during cycling. Lithium was electrochemically deposited in a half cell onto the surface of one of the electrodes to a charge of 6 mA h cm⁻² at a current density of 0.5 mA cm⁻². After Li deposition, these electrodes were labelled as Li@C and Li@TiC@C2, and were placed into a cell with a bare C or TiC@C2 (respectively) electrode and an ether-based electrolyte. The voltage–time profiles of the symmetric cells were collected with a Li plating/stripping capacity of 0.5 mA h cm⁻² under a current density of 0.5 mA cm⁻² (Fig. 6a). The Li@TiC@C2 symmetric cell exhibited excellent cycling stability with a small voltage hysteresis (~8 mV) over more than 180 cycles. In contrast, the Li@C symmetric cells showed a gradual overpotential rise during repeated plating and stripping, especially after the 50th cycle, which is mainly ascribed to the formation of dead lithium and the lithiophobic nature of the carbon surfaces (Fig. 6b and e). Similarly, when employed at a higher current of 1 mA cm⁻² (Fig. S9†), the Li@TiC@C2 symmetric cell displays stable voltage overpotential for more than 1000 h, which is much better than that of Li@C symmetric cell. Such significant improvement is mainly attributed to the enlarged surface area of self-standing TiC@C electrode and lithiophilic modification of TiC.

Electrochemical impedance spectroscopy (EIS) measurements following different numbers of charge–discharge cycles can be used to further explore the interfacial resistance. All EIS tests were conducted in half cells with a bare carbon or TiC@C2 working electrode against Li foil. Before cycling, the bare C exhibits a slightly larger charge-transfer resistance ($R_{ct} = 37 \Omega$) than that of TiC@C2 ($R_{ct} = 33 \Omega$), as shown in Fig. S10a (ESI†), which is consistent with the lower lithiophilicity of the bare C. In Fig. 7 and Table 2, after 10 cycles, the impedance of the TiC@C2 cell ($R_{ct} = 15.5 \Omega$) is slightly bigger than that of the bare C cell ($R_{ct} = 9.9 \Omega$). However, following 50 cycles, the impedance of the TiC@C2 cell ($R_{ct} = 14.7 \Omega$) is obviously smaller than that of the C cell ($R_{ct} = 20.6 \Omega$), indicating a significantly quicker kinetic process resulting from the introduction of TiC. The resistance value of the TiC@C2 cell fluctuates by just 5%, while the HC cell's resistance value varies by 40%. The R_s and R_{ct} values of the TiC@C2 cell are gradually decreased upon cycling within 50 cycles, indicating a progressive stabilising process, while those of the C cell increased, signifying uncontrolled generation of dead Li and fracture of the SEI film.

To illustrate that the TiC@C has the potential to be useful in practical applications, full cells were assembled with Li@TiC@C2, Li@C or Li foil as anodes and LiFePO₄ (~1.68 mg

cm⁻²) as cathode. Fig. 8a shows the charge–discharge profiles of different full cells at 1C. This fast charge/discharge rate was used to increase the likelihood of Li dendrite production. Compared with the Li full cell, the polarisation between the charge and discharge plateaus for the Li@C full cell exhibits a decrease from 116 to 92 mV, while the polarisation of Li@TiC@C provides a further decrease to 52 mV, indicating that the kinetics of the Li@TiC@C full cell are significantly improved (Fig. 8b). Meanwhile, as expected, the Li@TiC@C–LFP full cell delivered the best performance and provided a reversible capacity of 130 mA h g⁻¹ at 1C after 250 cycles, while the specific capacities of the Li@C/LFP and Li/LFP full cells are only 122 mA h g⁻¹ and 50 mA h g⁻¹ (Fig. 8c), respectively. This significant improvement in cycle performance supports the benefits of TiC in uniform Li nucleation for creating dendrite-free and long-term stable Li anodes. Importantly, there is limited Li in the Li@TiC@C2 electrode, which is only one-twelfth of that in the Li foil (calculation of which can be found in ESI†). The CE performances of full cells with LFP cathode against Li, C@Li, and TiC@C@Li are also provided in Fig. S11.† The first CE of the TiC@C@Li/LFP full cell (99.77%) is higher than that of the C@Li/LFP full cell (98.70%) and the Li/LFP full cell (98.38%), and the CE of the TiC@C@Li/LFP full cell is 99.70% after 450 cycles. This further proved that TiC@C@Li can effectively regulate the Li plating/stripping process and inhibit the formation of Li dendrites and dead Li. The rate performances of different anodes were also measured from 1C to 5C (Fig. 8d). The Li@TiC@C/LFP full cell also exhibits better rate performances than the other cell systems when coupled with a LiFePO₄ cathode, especially at higher rates. The discharge capacity of the TiC@C@Li/LFP full cell is 157 mA h g⁻¹ at low current density (1C), which is almost the same as that of the C@Li/LFP full cell (155 mA h g⁻¹ at 1C). However, with higher current density (5C), the TiC@C@Li/LFP full cell provides a higher capacity of 128 mA h g⁻¹ than that of the C@Li/LFP full cell (120 mA h g⁻¹ at 5C), while the specific capacity of the Li/LFP full cell is only 85 mA h g⁻¹. The corresponding charging/discharging profile of 5C also exhibits an obvious reduction of voltage polarization between the TiC@C@Li/LFP full cell and the Li/LFP full cell, which further confirms the faster kinetics of the TiC@C@Li/LFP full cell.

Conclusions

A TiC-modified 3D carbon network has been designed and prepared as a lithium metal host to suppress the formation of lithium dendrites in lithium metal batteries. Half-cells with TiC@C electrodes can cycle for more than 200 cycles with a current density of 2 mA cm⁻² and a plating areal capacity of 1 mA h cm⁻², maintaining a high and stable average coulombic efficiency (~99.6%). Furthermore, the overpotential decreased significantly when lithium metal was deposited on the TiC@C composite electrode (–60 mV). The lithiophilic TiC increases the affinity between the entire 3D electrode and lithium, reducing the local current density and providing a large number of lithium metal nucleation sites to induce a uniform distribution and deposition of lithium metal. Consequently, the cell



performance improved significantly compared with an unmodified carbon network. This work provides new insights into the design of 3D lithium hosts with sustainable carbon skeletons for high-performance lithium metal anodes and cost-effective carbon-based composites for the lithium metal batteries.

Data availability

Raw data used to prepare the figures in the article and ESI† are available from the University of Southampton repository at <https://doi.org/10.1039/D3TA01707A>.

Conflicts of interest

There are no conflicts to declare.

Acknowledgements

JW thanks the China Scholarship Council for funding. The authors also thank EPSRC for funding equipment used in this work under EP/K00509x/1, EP/K009877/1 and EP/V007629/1, and Nikolay Zhelev for SEM training and help with imaging the morphology of Li dendrites.

References

- 1 M. Armand and J. M. Tarascon, *Nature*, 2008, **451**, 652–657.
- 2 Y. Zhang, T. T. Zuo, J. Popovic, K. Lim, Y. X. Yin, J. Maier and Y. G. Guo, *Mater. Today*, 2020, **33**, 56–74.
- 3 D. Lin, Y. Liu, A. Pei and Y. Cui, *Nano Res.*, 2017, **10**, 4003–4026.
- 4 S. S. Zhang, *ACS Appl. Energy Mater.*, 2018, **1**, 910–920.
- 5 H. Zhang, G. G. Eshetu, X. Judez, C. Li, L. M. Rodriguez-Martínez and M. Armand, *Angew. Chem., Int. Ed.*, 2018, **57**, 15002–15027.
- 6 Q. Yang, N. Deng, J. Chen, B. Cheng and W. Kang, *Chem. Eng. J.*, 2021, **413**, 127427.
- 7 S. Lou, F. Zhang, C. Fu, M. Chen, Y. Ma, G. Yin and J. Wang, *Adv. Mater.*, 2021, **33**, 2000721.
- 8 M. D. Tikekar, S. Choudhury, Z. Tu and L. A. Archer, *Nat. Energy*, 2016, **1**, 1–7.
- 9 J. Lang, Y. Long, J. Qu, X. Luo, H. Wei, K. Huang, H. Zhang, L. Qi, Q. Zhang and Z. Li, *Energy Storage Mater.*, 2019, **16**, 85–90.
- 10 S. S. Chi, Y. Liu, W. L. Song, L. Z. Fan and Q. Zhang, *Adv. Funct. Mater.*, 2017, **27**, 1700348.
- 11 Q. Li, S. Zhu and Y. Lu, *Adv. Funct. Mater.*, 2017, **27**, 1606422.
- 12 L. Liu, Y. X. Yin, J. Y. Li, N. W. Li, X. X. Zeng, H. Ye, Y. G. Guo and L. J. Wan, *Joule*, 2017, **1**, 563–575.
- 13 Z. Sun, S. Jin, H. Jin, Z. Du, Y. Zhu, A. Cao, H. Ji and L. J. Wan, *Adv. Mater.*, 2018, **30**, 1800884.
- 14 W. Deng, W. Zhu, X. Zhou and Z. Liu, *Energy Storage Mater.*, 2018, **15**, 266–273.
- 15 C. Jin, O. Sheng, W. Zhang, J. Luo, H. Yuan, T. Yang, H. Huang, Y. Gan, Y. Xia and C. Liang, *Energy Storage Mater.*, 2018, **15**, 218–225.
- 16 Z. Lin, S. Li and J. Huang, *Chem. Rec.*, 2020, **20**, 187–208.
- 17 K. Yan, Z. Lu, H.-W. Lee, F. Xiong, P.-C. Hsu, Y. Li, J. Zhao, S. Chu and Y. Cui, *Nat. Energy*, 2016, **1**, 1–8.
- 18 C. Yang, Y. Yao, S. He, H. Xie, E. Hitz and L. Hu, *Adv. Mater.*, 2017, **29**, 1702714.
- 19 R. Zhang, X. R. Chen, X. Chen, X. B. Cheng, X. Q. Zhang, C. Yan and Q. Zhang, *Angew. Chem.*, 2017, **129**, 7872–7876.
- 20 Z. Wen, H. Li, J. Liu, Y. Yang and J. Zhao, *ACS Sustainable Chem. Eng.*, 2021, **9**, 2326–2337.
- 21 K. Lin, X. Qin, M. Liu, X. Xu, G. Liang, J. Wu, F. Kang, G. Chen and B. Li, *Adv. Funct. Mater.*, 2019, **29**, 1903229.
- 22 L. Zhao, W. Wang, X. Zhao, Z. Hou, X. Fan, Y. Liu and Z. Quan, *ACS Appl. Energy Mater.*, 2019, **2**, 2692–2698.
- 23 Y. Liu, S. Zhang, X. Qin, F. Kang, G. Chen and B. Li, *Nano Lett.*, 2019, **19**, 4601–4607.
- 24 Y. Zhang, C. Wang, G. Pastel, Y. Kuang, H. Xie, Y. Li, B. Liu, W. Luo, C. Chen and L. Hu, *Adv. Energy Mater.*, 2018, **8**, 1800635.
- 25 S. Liu, X. Xia, Y. Zhong, S. Deng, Z. Yao, L. Zhang, X. B. Cheng, X. Wang, Q. Zhang and J. Tu, *Adv. Energy Mater.*, 2018, **8**, 1702322.
- 26 B. Yu, D. Chen, Z. Wang, F. Qi, X. Zhang, X. Wang, Y. Hu, B. Wang, W. Zhang and Y. Chen, *Chem. Eng. J.*, 2020, **399**, 125837.
- 27 S. Park, H. J. Jin and Y. S. Yun, *Adv. Mater.*, 2020, **32**, 2002193.
- 28 G. Yang, Z. Liu, S. Weng, Q. Zhang, X. Wang, Z. Wang, L. Gu and L. Chen, *Energy Storage Mater.*, 2021, **36**, 459–465.
- 29 X.-B. Cheng, J.-Q. Huang and Q. Zhang, *J. Electrochem. Soc.*, 2017, **165**, A6058.
- 30 H. Cheng, N. Garcia-Araez, A. L. Hector and S. Soulé, *Inorg. Chem.*, 2019, **58**, 5776–5786.
- 31 H. Cheng, N. Garcia-Araez and A. L. Hector, *ACS Appl. Energy Mater.*, 2020, **3**, 4286–4294.
- 32 C. Jin, O. Sheng, J. Luo, H. Yuan, C. Fang, W. Zhang, H. Huang, Y. Gan, Y. Xia and C. Liang, *Nano Energy*, 2017, **37**, 177–186.
- 33 W. Xu, J. Wang, F. Ding, X. Chen, E. Nasybulin, Y. Zhang and J. G. Zhang, *Energy Environ. Sci.*, 2014, **7**, 513–537.
- 34 R. Zhang, X. B. Cheng, C. Z. Zhao, H. J. Peng, J. L. Shi, J. Q. Huang, J. Wang, F. Wei and Q. Zhang, *Adv. Mater.*, 2016, **28**, 2155–2162.
- 35 Z. Wen, H. Li, J. Liu, Y. Yang and J. Zhao, *ACS Sustainable Chem. Eng.*, 2021, **9**, 2326–2337.
- 36 Y. Chen, A. Elangovan, D. Zeng, Y. Zhang, H. Ke, J. Li, Y. Sun and H. Cheng, *Adv. Funct. Mater.*, 2020, **30**, 1906444.
- 37 A. Pei, G. Zheng, F. Shi, Y. Li and Y. Cui, *Nano Lett.*, 2017, **17**, 1132–1139.
- 38 K. Yan, H. W. Lee, T. Gao, G. Zheng, H. Yao, H. Wang, Z. Lu, Y. Zhou, Z. Liang and Z. Liu, *Nano Lett.*, 2014, **14**, 6016–6022.
- 39 J. Cui, S. Yao, M. Ihsan-Ul-Haq, J. Wu and J. K. Kim, *Adv. Energy Mater.*, 2019, **9**, 1802777.

